Arabian Journal of Chemistry (2020) **13**, 7403–7417

King Saud University

Arabian Journal of Chemistry

www.ksu.edu.sa
www.sciencedirect.com

ORIGINAL ARTICLE

Magnetic properties, anticancer and antibacterial effectiveness of sonochemically produced Ce^{3+}/Dy^{3+} co-activated Mn-Zn nanospinel ferrites

M.A. Almessiere [a,*], Y. Slimani [a,*], S. Rehman [b], F.A. Khan [c], Ç.D. Güngüneş [d], S. Güner [e], Sagar E. Shirsath [f], A. Baykal [g]

[a] *Department of Biophysics, Institute for Research and Medical Consultations (IRMC), Imam Abdulrahman Bin Faisal University, P. O. Box 1982, Dammam 31441, Saudi Arabia*
[b] *Department of Epidemic Disease Research, Institute for Research and Medical Consultations (IRMC), Imam Abdulrahman Bin Faisal University, P.O. Box 1982, Dammam 31441, Saudi Arabia*
[c] *Department of Stem Cell Biology, Institute for Research and Medical Consultations (IRMC), Imam Abdulrahman Bin Faisal University, P.O. Box 1982, Dammam 31441, Saudi Arabia*
[d] *Department of Nutrition and Dietetics, Faculty of Health Science, Hitit University, 19030 Çevreyolu Bulv., Çorum, Turkey*
[e] *Institute of Inorganic Chemistry, RWTH Aachen University, D-52074 Aachen, Germany*
[f] *School of Materials Science and Engineering, University of New South Wales, Kensington, Sydney, NSW 2052, Australia*
[g] *Department of Nano-Medicine Research, Institute for Research and Medical Consultations (IRMC), Imam Abdulrahman Bin Faisal University, P.O. Box 1982, Dammam 31441, Saudi Arabia*

Received 5 June 2020; accepted 16 August 2020
Available online 25 August 2020

KEYWORDS

Nanospinel ferrites;
Sonochemistry;
Anti-cancerous application;
Bactericidal application;
Magnetic properties;
Morphology

Abstract Some new types of Ce^{3+} and Dy^{3+} co-doped manganese-zinc nanospinel ferrites (CDMZNSFs) of the form $(Mn_{0.5}Zn_{0.5})[Fe_{2-2x}Ce_xDy_x]O_4$ (with $0.0 \leq x \leq 0.1$) were sonochemically produced and characterized. The structure, morphology, optical and magnetic properties of these NSFs were determined as a function of co-dopant (Ce^{3+} and Dy^{3+}) contents. The direct optical band gap energies of the studied NSFs were ranged from 1.54 to 1.85 eV. The measurements of magnetization versus magnetic field of the prepared NSFs disclosed a superparamagnetic (SPM) behavior at room temperature (RT). The measurements of temperature-dependent magnetizations revealed a transition from superparamagnetic (SPM) state above blocking temperature T_B to a ferromagnetic (FM) state below T_B. The saturation magnetization and T_B decreased with the increase in co-dopant contents. In addition, the bactericidal (on the gram-positive and gram-negative bac-

* Corresponding authors.
E-mail addresses: malmessiere@iau.edu.sa (M.A. Almessiere), yaslimani@iau.edu.sa, slimaniyassine18@gmail.com (Y. Slimani).
Peer review under responsibility of King Saud University.

Production and hosting by Elsevier

https://doi.org/10.1016/j.arabjc.2020.08.017

terial strains) and anti-cancerous effectiveness of these NSFs were assessed. The cancer cells' growth inhibitory action of these NSFs was tested against both normal (HEK-293) and cancerous (HCT-116) human cells. After 48 h of treatment of the cancerous cells with the NSFs, their population was significantly dropped as shown by the MTT assay, indicating the selective inhibition of the cancer cells growth by the proposed NSFs. Conversely, the non-cancerous cells (HEK-293) population remained unaffected. The IC_{50} values of the NSFs-treated cancerous cells (HCT-116) were in the range of 0.74–2.35 μg/mL. The results of the MIC and MBC assays revealed the reasonable antibacterial efficacy (growth inhibitory activity) of these NSFs when tested against the *E. coli* and *S. aureus* bacterial strains. It is established that the proposed Ce^{3+}/Dy^{3+} co-activated CDMZNSFs may be beneficial for the anti-cancerous and bactericidal applications.

1. Introduction

The novel spinel ferrites became the most active research areas due to numerous manufacturing such as data storage, radar absorbing, telecommunication, negligible eddy current losses, microwave, permanent magnets, refractory materials, sensors, ferro-fluids, hydrogen production, decomposition of alcohols, oxidative dehydrogenation, electro-catalytic activity and corrosion resist (Joulaei et al., 2019; Kiani et al., 2019; Eskandari et al., 2019; Etminan et al., 2018; Moradi et al., 2018; Naghikhani et al., 2018). Lately, the Mn-Zn spinel ferrites (MZSFs, the soft ferromagnetic ceramic materials) due to their exclusive electrical, magnetic and optical properties have widely been used in the communication, home appliances, computer, cores of inductors, transformers, recording heads, hyperthermia devices, cancer cells treatment, magnetic resonance imaging (MRI) and so forth (Hu et al., 2010; Xing et al., 2012; Ahmed et al., 2007; Parekh et al., 2006). In-depth studies disclosed that all these unusual characteristics of the MZSFs are decided by preferred distributions of the Fe^{3+} and Fe^{2+} cations into the tetrahedral and octahedral sub-lattice sites in the crystal structure (Ahmed et al., 2007), where the syntheses techniques of these ferrites play a significant role.

The crystal unit cell of the MZSFs encloses sixty-four tetrahedral lattice positions (A-sites) and thirty-two octahedral lattice positions (B-sites), where the metal cations occupy eight A-lattice sites and sixteen B-lattice sites, leaving seventy-two positions vacant. Consequently, the unoccupied lattice sites in crystalline unit cells of the MZSFs can accommodate various metal ions such as the trivalent lanthanides, causing a modification in their structural, optical, and magnetic characteristics (Modak et al., 2009). The present study is motivated by the possibilities where rare earth ions co-doped new types of low dimensional MZSFs with improved traits can be composed for novel applications.

To fulfill the ever-increasing demand of the high-quality MZSFs, numerous syntheses strategies have been adopted such as the co-precipitation (Mathur et al., 2007), polyol process (Topfer and Angermann, 2011), hydrothermal (Akhtar et al., 2019), solid-state reaction (Kogias and Zaspalis, 2016), sonochemical (Almessiere et al., 2020; Rehman et al., 2020), auto-combustion (Baykal et al., 2015) and so on. Recent studies showed that using the ultrasonic waves at high intensity some good quality MZSFs nanostructures (doped and undoped) with customized properties can be achieved. Amongst all these techniques the sonochemical strategy is advantageous due to its ability to form nanocomposites of uniform sizes rapidly with less energy consumption and fast reaction rates (Asgharzadehahmadi et al., 2016; Pinjari and Pandit, 2011). On top, the sonochemical technique being relatively simple, accurate, and economic, it can produce contaminant-free Mn-Zn nanospinel ferrites (MZNSFs) at a large scale in short duration compared to the conventional approaches. In this view, we used this approach to prepare Ce^{3+}/Dy^{3+} co-activated MZNSFs (CDMZNSFs).

According to Rezlescu et al. (1998); the trivalent rare earth impurities due to their large ionic radii and exceptional 4f shell electronic configurations can be the excellent substituents in the lattice structures of the soft MZNSFs, thereby improving their structural, optical, magnetic and electrical traits. The rare earth ions substitutions in the MZNSFs leads to the development of a strong exchange coupling between the 4f and 3d electrons, contributing to the significant magneto-crystalline anisotropy in the spinel structures and physical properties improvement (Islam et al., 2013; Song et al., 2010; Almessiere et al., 2019; Ateia et al., 2020). Mohd. Hashim and et al. investigated the Structural, optical, elastic and magnetic features of $CoCe_xDy_xFe_{2-2x}O_4$ (x = 0.0, 0.01, 0.02, 0.03, 0.04, 0.05) were fabricated by sol gel auto combustion technique. They found that the blocking temperatures at x = 0.00, 0.03 and 0.05 higher than room temperature and reductions with growing the Ce and Dy ratio. The higher values of saturation magnetism and Hyperfine field for x = 0.01 composition may be due to the all Dy^{3+} ions occupy at octahedral site while the Ce^{3+} ions might be occupied at tetrahedral site. As the doping amount increases, the saturation magnetism decreases noticeably, and this attributable to the replacement of iron by these doping ions (Hashim et al., 2020). While A.A. Kadam and et al. studied the Structural, morphological, electrical and magnetic characteristics of dysprosium doped Ni0.8Co0.2Fe2-xDyxO4 ferrite prepared by simple ceramic process. The samples showed a reduction in dielectric constant, loss tangent and ac conductivity with frequency. Moreover, low coercive field suggested that these ferrites can be used in magnetic shielding devices (Kadam et al., 2013). Le-Zhong Li and et al. explored the structural and electromagnetic propertiesNi0.4Zn0.6 − xCexFe2O4 ($0 \leq x \leq 0.20$) were synthesized via the sol-gel combing with the solid reaction procedure. They observed that the saturation magnetism (Ms) initially increases with increasing amount of Ce substitution due to the increase of density and reduction of

porosity, and decreases when Ce substitution excessed 0.15 that contributes to the increase of the net magnetic moment in tetrahedral site and porosity and the presence of CeO2 phase. The initial permeability firstly increases at room temperature with the Ce substitution content increasing and reach the maximum at x = 0.15. However, it sharply drops when the amount of Ce replacement is 0.20 because the porosity increasing and impurity phase appearance (Li et al., 2019). Shirsath et al. (2011) reported Ce substituted $NiFe_2O_4$ ferrite prepared by solid-state reaction. Ce4+ increased the pore mobility in $NiFe_2O_4$ ferrite by creating excess cation vacancies affecting overall grain growth and bulk density. Moreover, higher magnetocrystalline anisotropy associated with rare earth Ce^{4+} ions promoted the enhancement in coercivity.

In this perception, we used the sonochemical method to synthesize some new types of MZNSFs with Ce^{3+} and Dy^{3+} co-substitutions for the first time. As-prepared CDMZNSFs were characterized using diverse tools to determine the role of varying Ce^{3+} and Dy^{3+} contents on their structural, morphological, optical and magnetic features. In addition, the anticancer and anti-bacterial efficacy of the produced CDMZNSFs was tested against the human cells (normal HEK-293 and cancerous HCT-116) and bacterial strains (*Escherichia coli* and *Staphylococcus aureus*).

2. Experimental

2.1. Synthesis and characterizations of Ce^{3+} and Dy^{3+} co-doped MZNSFs

A series of MZNSFs co-activated with Ce^{3+}/Dy^{3+} impurities were produced using the sonochemical route. First, the high purity chemical reagents (from Merck) of [$MnCl_2{\cdot}4H_2O$] (manganese II chloride), [$Zn(NO_3)_2$] (zinc nitrate), [$Dy(NO_3)_3{\cdot}H_2O$] (dysprosium III nitrate hydrate), [$Fe(NO_3)_3{\cdot}9H_2O$] (Iron (III) nitrate nonahydrate) and [$Ce(NO_3)_3{\cdot}6H_2O$] (cerium nitrate hexahydrate) were mixed in deionized water (DIW). The pH of the resultant mixture was adjusted to 11 via the addition of 2 M of NaOH solution before being irradiated ultrasonically for 30 min (UZ SONOPULS Ultrasonic Homogenizer HD 2070 operated at the frequency of 20 kHz and power of 70 W). Next, the solution containing the product was rinsed using DIW followed by the drying at 60 °C for nearly 24 h to achieve the solid samples. Finally, samples were characterized at room temperature using different analytical instruments.

The X-ray diffraction (XRD) analyses of the produced CDMZNSFs were performed (Rigaku Benchtop Miniflex X-ray Diffractometer operated with Cu-Kα radiation) to determine their crystalline structures and phase compositions. The surface morphologies of the prepared NSFs were evaluated using the scanning electron microscopy (SEM, FEI Titan ST). The elemental compositions of the samples were studied using the energy dispersive X-ray (EDX) spectroscopy (attached to SEM). The shape and size distributions of the CDMZNSFs were recorded using a transmission electron microscope (TEM, FEI Morgagni 268). The UV–Visible diffuse reflectance spectra (in the wavelength range of 200–800 nm) of the samples were obtained. The room temperature (RT, 300 K) magnetic measurements of the prepared samples were examined by using Quantum Design Physical Property Measurement System (PPMS DynaCool) coupled with a vibrating sample magnetometer (VSM) head in the applied magnetic field (H) range of ±7 Tesla. In addition, the measurements of magnetization versus temperature under zero-field-cooling (ZFC) and field-cooling (FC) modes were performed in the range of 300–10 K.

2.2. Anticancer activities

2.2.1. In vitro cytotoxicity assay

The colorectal carcinoma cells of human (HCT-116) were used to inspect the cancer cells inhibitory action of the as-prepared CDMZNSFs. Meanwhile, the normal (healthy) embryonic kidney cells of human (HEK-293) were used to assess the cytotoxicity of the CDMZNSFs. The earlier referred (Asgharzadehahmadi et al., 2016) protocols were used for the cells culture. The studied cells were cultivated at 37 °C in a carbon dioxide (CO_2) incubator inside the DMEM medium (Dulbecco's Modified Eagle's Medium) composed of the L-glutamine, fetal bovine serum, penicillin (antibiotic), selenium chloride and streptomycin. Upon reaching the confluence of 70–80%, the MTT [3-(4,5-dimethylthiazol-2-yl)-2,5-diphenyl tetrazolium bromide] assay (Molecules, New Zealand) was performed on the cultured cells to determine the anti-cancer viability of the proposed CDMZNSFs-treated at various doses (2.0 to 40 μg//mL) where the control group was devoid of NSFs. After treating the cells culture for a period of 48 h, the culture media was isolated and supplemented with the MTT solution of concentration 10 mg/mL (Sigma-Aldrich, USA) followed by further incubation of the plates enclosing cultures. Again, the cells culture medium was isolated and every well was supplemented with dimethyl sulfoxide (DMSO) in which MTT created Formazan crystallites. Later, the plates enclosing the CDMZNSFs-treated cells culture were analyzed (at wavelength of 570 nm) using the micro-plate readers (Bio-Rad Laboratories, USA). The mean and standard errors of both normal and CDMZNSFs-treated groups were scrutinized using the GraphPad Prism (GraphPad Software).

2.2.2. Nuclear staining by 4′,6-diamidino-2-phenylindole, DAPI) fluorescent dye

The DAPI (4′,6-diamidino-2-phenylindole) fluorescent dye (1.0 μg/mL) was used to stain the CDMZNSFs-treated cancer cells to discern their effects on the cell nuclei. The normal cells (HCT-116) in group-I were treated with CDMZNSFs and group-II was not treated. After 48 h of treatments using the CDMZNSFs, both non-cancerous (HCT-116) and cancerous (HEK-293) human cells were treated with 4% of paraformaldehyde prepared in phosphate buffer saline (PBS). Thereafter, the cells' membranes were permeabilized using Triton X-100-PBS treatment for 5 min. Finally, the DAPI staining of the cells was conducted in the darkroom. The nuclear morphologies of the cells were examined via a confocal scanning microscope (Zeiss, Germany) (Pinjari and Pandit, 2011).

2.3. Bactericidal activities

2.3.1. Synthesis of inoculum and stock solutions

To evaluate the antibacterial activities of the CDMZNSFs, the NSFs were homogenized using sterile distilled water to get the solution. The NSFs were added to the sterile Luria Bertani

(LB) broth at the concentration range of 16 to 0.5 mg/mL. The inoculum of *Escherichia coli* (ATCC35218, gram-negative) and *Staphylococcus aureus* (ATCC29213, gram-positive) bacteria was prepared using the LB broth after the incubation at 35 ± 2 °C for overnight. The cell densities (2.5×10^6 CFUs/mL) of the freshly cultured bacterial strains were adjusted by the addition of sterile Luria Bertaini broth (Rezlescu et al., 1998).

2.3.2. Minimal inhibitory concentration (MIC)

The MIC values of the prepared CDMZNSFs solutions were determined using the broth dilution method after supplementing the freshly adjusted bacterial inoculum (density of 2.5×10^5 CFU/mL) with incubation in air for 24 h at 35 ± 2 °C. The solution without bacterial treatment was considered as the negative control. The MIC record was chosen as the minimal drug content at which no growth was visually seen, indicating the absence of turbidity.

2.3.3. Minimum antibacterial concentration (MBC)

After the MIC of evaluation of the CDMZNSFs solutions, the aliquot of suspension was withdrawn without causing any turbidity followed by the inoculation on freshly made Mueller Hinton Agar (MHA) plate with further incubation for 24 h at 35 ± 2 °C. The MBC of the drug was recorded as the lowermost content without bacterial cells or below 3 CFU on the MHA plate.

2.3.4. Morphology characterization of CDMZNSFs-treated bacteria

The effect of CDMZNSFs on the morphologies of the bacterial cells (gram positive and negative) was examined via SEM imaging. Both bacterial strains (10^6 CFU/mL) were treated at the concentration obtained as MIC value of the particular NSFs with the overnight incubation at 37 ± 2 °C wherein the bacteria without NSFs treatment were taken as the control. Upon completing the incubation, the bacterial cells were centrifuged and washed repeatedly using the PBS. Thereafter, the bacterial cells were treated for 4 h using the glutaraldehyde (2.5%) followed by the fixing via osmium tetroxide (1%). Then, the resultant samples were rinsed and dried using ethanol at different concentrations. Next, the bacterial cells were put on the Al stubs and dried inside the desiccator followed by the Au coating for the SEM measurements (Ateia et al., 2020).

3. Results and discussion

3.1. Structural analyses of CDMZNSFs

The formation of phases in the CDMZNSFs ($0.0 \leq x \leq 0.1$) was observed via the XRD powder pattern as shown in Fig. 1. The reflection planes for all the samples were found belong to the typical pure single phase of the MZNSFs correspond to h k l planes of (220), (311), (222),(400), (422) (511) and (440) respectively without any other phase of the metals oxides according to card number [96-230-0619] and [96-101-0131]. The presence of intense diffraction peaks confirmed the presence of high crystallinity. The most intense peaks (311) of all the samples were broadened, indicating a decrease

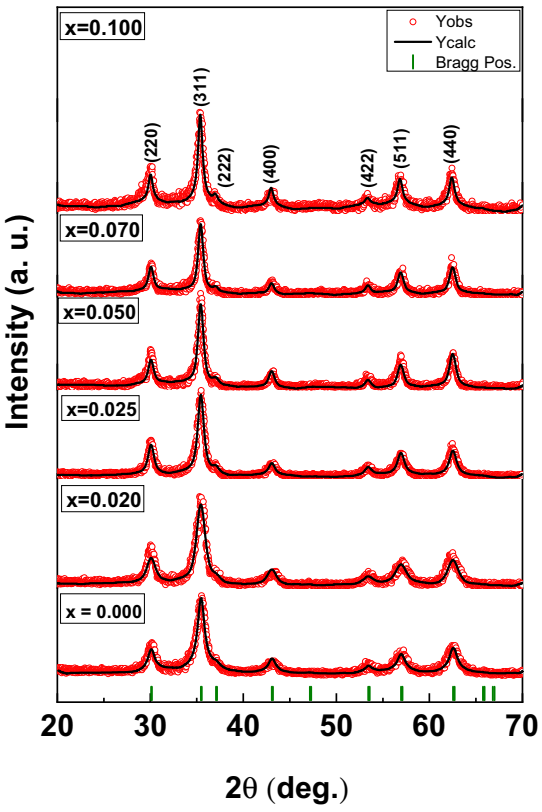

Fig. 1 The XRD patterns of the studied CDMZNSFs ($0.0 \leq x \leq 0.1$).

in the average crystallite size. The Rietveld refinement using (Match3! and fullproof) was used to estimate the lattice constant (*a*) and average crystallite size as listed in Table 1.The values of lattice constant (*a*) and unit cell volume (V) were found increase with increasing the co-dopant (Ce^{3+}/Dy^{3+}) concentration which was due to their larger ionic radii Ce^{3+} (1.01 Å), Dy^{3+} (0.91 Å) than the Fe^{3+} ions (0.64 Å), generating a deformation in the spinel ferrite lattice to recompense the developing strain and stress (Parekh et al., 2006). The crystallite size was estimated via Scherrer formula by considering the most intense plane (3 1 1) and it was found in the range from 8.6 to 18.5 nm (Table 1).

The cations distribution in the CDMZNSFs crystalline unit cells was determined by analyzing the XRD data via the Bertaut technique as shown in Table 2 (Shirsath et al., 2013, 2014). The majority of the Fe^{3+} occupied the octahedral sites (B-sublattice position) with few at the tetrahedral sites (A-sublattice position). Approximately 70–84% of the Mn^{3+} occupied the A-sites and 30–16% was distributed on the B-sites consistent with the preferential occupation at the tetrahedral sites (Shirsath et al., 2018). The Zn^{2+} showed the strong preferential occupation towards the tetrahedral A-sites as expected. Meanwhile, the Ce^{3+}/Dy^{3+} substituents preferentially occupied the octahedral B-sites only due to their larger ionic radii compared to the host metallic ions. A close investigation of XRD patterns confirmed the single phase formation of the prepared samples without forming the secondary phases of $DyFeO_3$, $CeFeO_3$, CeO and DyO. Further, lattice constant increased throughout the substitution range of Ce and Dy

Table 1 The structural properties of the studied CDMZNSFs ($0.0 \leq x \leq 0.1$).

x	A (Å)	V (Å)^3	$D_{XRD} \pm 0.04$ (nm)	χ^2	R_{Bragg}
0.000	8.3977	592.2151	18.5	1.2	13.2
0.020	8.4018	593.0809	11.3	1.1	10.4
0.025	8.4027	593.2673	10.8	1.3	12.7
0.050	8.4053	593.8287	10.4	1.2	15.9
0.070	8.4069	594.1721	9.6	1.0	13.9
0.100	8.4167	596.2524	8.6	1.1	17.8

Table 2 Cations distribution in the CDMZNSFs ($0.0 \leq x \leq 0.1$) unit cell.

x	Tetrahedral position (A-sites)	Octahedral position (B-sites)
0.000	$Mn_{0.35}Zn_{0.5}Fe_{0.15}$	$Mn_{0.15}Fe_{1.85}$
0.020	$Mn_{0.35}Zn_{0.5}Fe_{0.15}$	$Mn_{0.15}Dy_{0.02}Ce_{0.02}Fe_{1.81}$
0.025	$Mn_{0.36}Zn_{0.5}Fe_{0.14}$	$Mn_{0.14}Dy_{0.025}Ce_{0.025}Fe_{1.8}$
0.050	$Mn_{0.38}Zn_{0.5}Fe_{0.12}$	$Mn_{0.12}Dy_{0.05}Ce_{0.05}Fe_{1.78}$
0.070	$Mn_{0.4}Zn_{0.5}Fe_{0.1}$	$Mn_{0.1}Dy_{0.07}Ce_{0.07}Fe_{1.75}$
0.100	$Mn_{0.42}Zn_{0.5}Fe_{0.08}$	$Mn_{0.08}Dy_{0.1}Ce_{0.1}Fe_{1.72}$

ions. Thus, it can be concluded that Ce and Dy ions enters into to the crystal lattice of CDMZNSFs and occupied octahedral B-site because of their larger ionic radii.

3.2. Morphologies of CDMZNSFs

Fig. 2 displays the FESEM micrographs of the prepared CDMZNSFs (x = 0.000, 0.020, 0.050 and 0.100), which were comprised of the nonuniformly aggregated spherical nanocrystallites with the average size around 20 nm. Fig. 3 shows the TEM images of the studied CDMZNSFs (x = 0.025 and 0.100) which were contained of strong agglomerated nearly spherical nanocrystallites, supporting the FESEM observations. Moreover, the HRTEM images of CDMZNSFs (x = 0.025 and 0.100) are consisted of well resolved two-dimensional lattice spaces with of 0.25 nm, 0.29 nm and 0.19 nm corresponding to lattice plane (311), (220) and (331), respectively for Mn-Zn spinel ferrites. The SAED pattern displayed the well-separated dotted rings indicating the crystalline nature of the particles. The first six rings of the SAED patterns were labelled as, (220), (311), (400), (422), (511) and (440). The maximum intensity was obtained for (311) reflection which is consistent with the XRD pattern as shown above by Fig. 1. Fig. 4 illustrates the EDX spectra of the achieved CDMZNSFs, verifying the appropriate elemental compositions (Mn, Zn, Dy, Fe, Ce and O) of the samples. EDS color mapping analysis (Fig. 4) confirmed that the Ce and Dy ions are uniformly distributed without forming a cluster. Thus, this is a further evidence that Ce and Dy ions indeed are in the crystalline grain and not on the grain boundary.

3.3. Optical band gap energy

Optical band gap energy (E_g) is a decisive property of semiconductors for optoelectronic applications. UV–vis diffuse reflectance spectroscopy (DRS) is one of the most employed methods for the determination of the optical bandgap of nanoparticle sized semiconducting substances. Fig. 5 shows the percent diffuse reflectance (DR %) spectra of the synthesized CDMZNSFs (Baykal et al., 2015; Güner et al., 2015). Spectra were recorded by a UV–vis spectrophotometer equipped with an integrating sphere between 200 nm and 800 nm of wavelength. The spectral peaks have appeared in the wavelength region between 200 and 500 nm with the intensity values in a narrow range of 13.40–15.70 %. Above 500 nm, we observe a sharp increase at reflectance intensities and among all the NSFs $Mn_{0.5}Zn_{0.5}Ce_{0.10}Dy_{0.10}Fe_2O_4$ showed a maximum reflectance intensity of 28.8% corresponding to 800 nm.

The DR spectral data were analyzed using the radiative transfer model introduced by Kubelka-Munk (K-M). In this model, the function $F(R_\infty)$ is defined as (Blitz, 1998):

$$F(R_\infty) = \frac{(1-R_\infty)^2}{2R_\infty} = \frac{K}{S} = \frac{2.303\varepsilon C}{S} \quad (1)$$

where R_∞ denotes the reflectance of the infinitely thick sample, ε is the absorptivity, K is the effective absorption coefficient, S is the effective scattering coefficient and C is the analyte contents. The K to S ratios (Blitz, 1998) characterizes the reflectance properties of the samples. The photon energy ($h\upsilon$) dependence of $F(R_\infty)$ can be approximated by the Tauc equation (Tauc et al., 1966; Baykal et al., 2018):

$$(F(R_\infty)h\upsilon)^n = A(h\upsilon - E_g) \quad (2)$$

where A is a constant and the exponent n signifies the nature of electronic transition across the band gap (direct or indirect) with n = 2 for the direct transition. The Tauc plot $(F(R_\infty)h\upsilon)^2$ versus $(h\upsilon)$) was generated to evaluate the values of E_g from the linear part of extrapolated line to$(F(R_\infty)h\upsilon)^2 = 0$.

Fig. 6 shows the Tauc plots of all the prepared CDMZNSFs. The value of E_g for the undoped MZNSFs was found to be 1.65 eV. The estimated values of E_g for the Dy^{3+}/Ce^{3+} co-doped MZNSFs were in the range of 1.65–1.77 eV, indicating the remarkable sensitiveness of the direct band gap energy of the NSFs on the co-dopant contents. All the prepared samples were semiconducting in nature. Some of the literature reports on the $Mn_{0.5}Zn_{0.5}Fe_2O_4$ NSFs prepared using hydrothermal and sonication assisted MW irradiation techniques revealed the corresponding E_g values of 1.98 and 1.99 eV (Nam et al., 2018; Ashok et al., 2019). In addition, other reports on the citric acid assisted sol-gel and thermal decomposition method grown $Mn_{1-x}Zn_xFe_2O_4$ MZNSFs (where x from 0.2 to 0.8) showed the E_g values in between

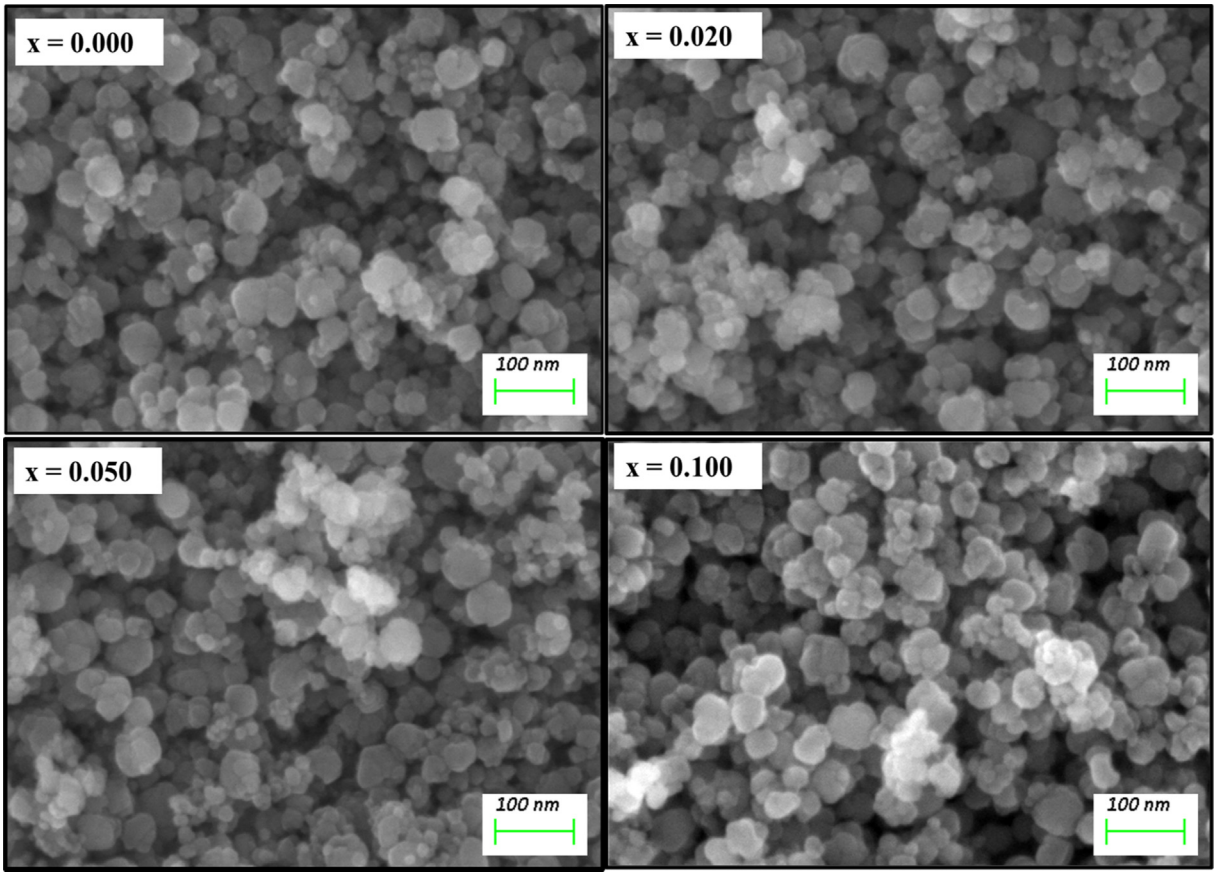

Fig. 2 The SEM images of the synthesized CDMZNSFs (x = 0.000, 0.020, 0.050 and 0.100).

1.86 and 2.80 eV (Baykal et al., 2015, 2014; Demir et al., 2014). Present work is the first report of the E_g values for the Dy^{3+}/Ce^{3+} co-substituted MZNSFs.

3.4. Magnetic properties

3.4.1. Magnetization versus magnetic field (M-H) hysteresis loops

Fig. 7 displays the RT hysteresis loops of all the prepared CDMZNSFs, which revealed superparamagnetic (SPM) behaviors. The measured M-H curves of all the samples revealed S-shape without any coercivity (H_c) and remanence (M_r). This behavior was due to the nucleation of the tiny NSF crystallites that could easily orient via the thermal activation, thereby overcoming the magnetic anisotropy (Chand et al., 2011). Essentially, the mean size of these crystallites was below the critical size (25 nm), thereby disclosing the predominant *SPM* phase (Lazarević et al., 2013; Almessiere et al., 2019; Zhang et al., 2009). This result was consistent with the XRD analyses that yield D_{XRD} values below 15 nm for various samples, confirming the crystallites sizes less than the critical limit (Table 1).

Since the magnetization of the prepared NSFs did not saturate completely (Fig. 7) despite the high magnetic field, the law of approach to saturation (LAS) at the higher field regions was applied in the M against $1/H^2$ plot (Fig. 8) for the selected undoped sample that enabled to estimate the values of the saturation magnetization (M_s) (Stoner and Wohlfarth, 1948; Almessiere et al., 2019).

Fig. 9 illustrates the variations in the M_s and magneton numbers (n_B) as a function of the Ce^{3+}/Dy^{3+} contents. The n_B values were calculated via (Almessiere et al., 2019a, 2019b):

$$n_B = \frac{Moleculor\ \ weight \times M_s}{5585} \quad (3)$$

The values of M_s and n_B for the undoped ($x = 0.0$) NSFs was 34.6 emu/g and 1.46 μ_B, respectively. The observed value of the M_s is lower than that of its bulk counterpart form (M_s-$\approx$ 140 emu/g) (Isfahani et al., 2009), which is mainly ascribed to the existence of the tinier crystallites that encountered the surface structural disorders, development of the magnetic inactive layers and spins canting (Coey, 1971; Slimani et al., 2019; Almessiere et al., 2019). Nevertheless, the value of M_s obtained here is higher than those recorded in other MZNSFs produced using co-precipitation (Parvatheeswara Rao et al., 2006), low-temperature solid-state reaction (Amiri et al., 2011), hydrothermal precipitation (Rath et al., 1999); evaporation and auto-combustion (Ranjith Kumar et al., 2013) and sol-gel combustion (Azadmanjiri, 2007) methods. In comparison to the pristine sample, the values of M_s of the NSFs are decreased with the rise in Ce^{3+} and Dy^{3+} contents.

Generally, the magnetic properties can be affected by various factors including the variations in the crystallites morphology (size and shape), the magnetic moments of the substituent and host ions, the strength of the super-exchange interactions, presence of disorder and inhomogeneities, etc. (Almessiere et al., 2019; Nairan et al., 2016). Several studies acknowledged the proportionality in the

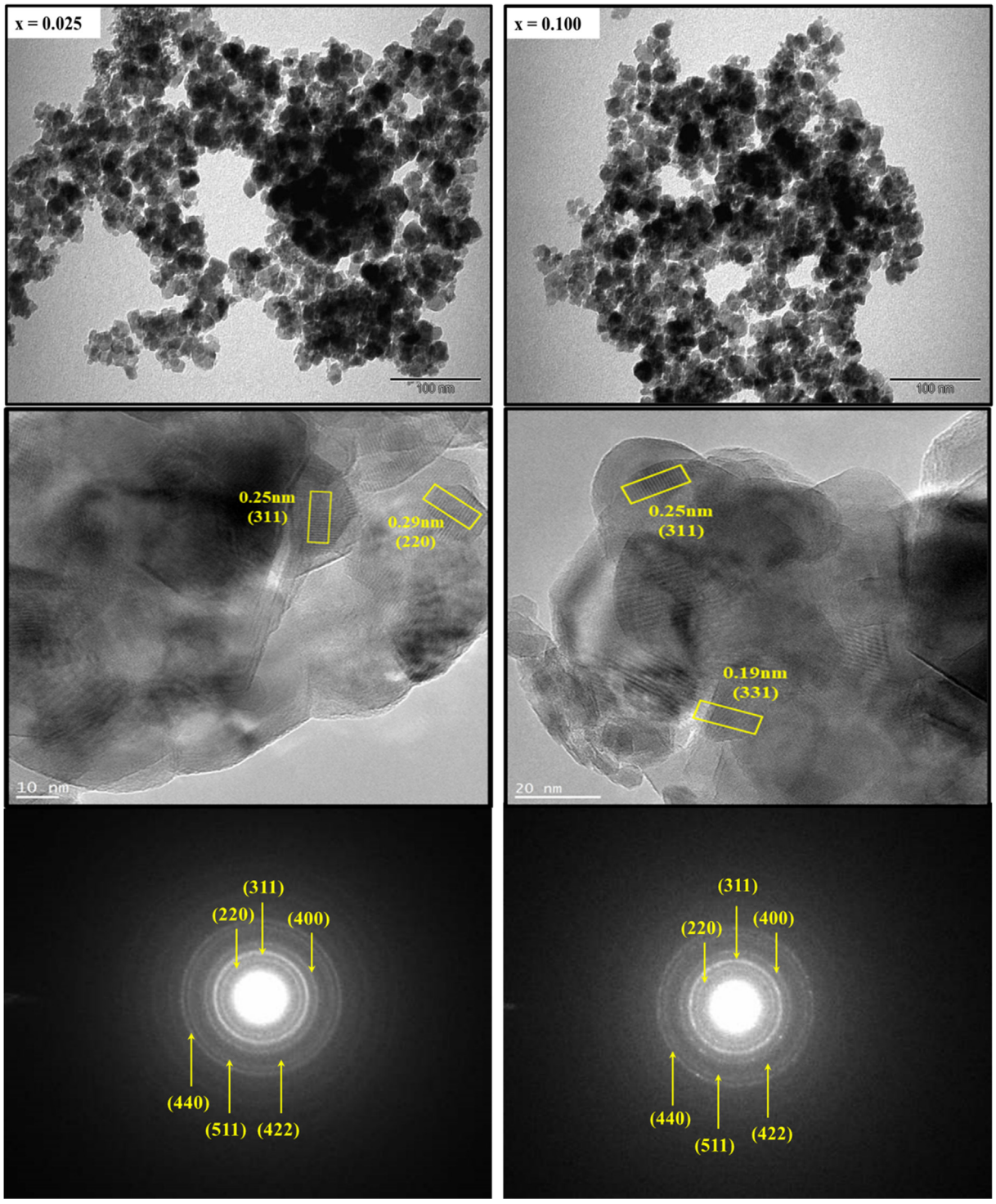

Fig. 3 The TEM, HR-TEM and SAED pattern of the synthesized CDMZNSFs (x = 0.025 and 0.100).

evolutions of crystallytes/grains size and M_s value (Almessiere et al., 2019; Nairan et al., 2016). Predominantly, the value of M_s increases with the increase of the crystallites/grains size and vice versa. As found in XRD part, the values of D_{XRD} are decreased with the increase in Ce^{3+} and Dy^{3+} contents, which are in line with the variations in M_s values. Furthermore, the dissimilarities in the ionic radii of Ce^{3+} (1.01 Å), Dy^{3+} (0.91 Å) and Fe^{3+} (0.64 Å) have a tendency to induce structural disorder, lattice strains and alteration in the electronic states into the prepared spinel ferrites, which in turn will affect on the magnetic parameters (Slimani et al., 2018). Additionally, the reduction in the magnetic moment (n_B) values signifies the weakening in the super-exchange interaction (Gabal et al., 2013; Almessiere et al., 2019). The variations of the n_B as function of Ce^{3+} and Dy^{3+} contents showed similar trend as that of M_s, indicating a weakening of the super-exchange interactions with Ce-Dy substitution.

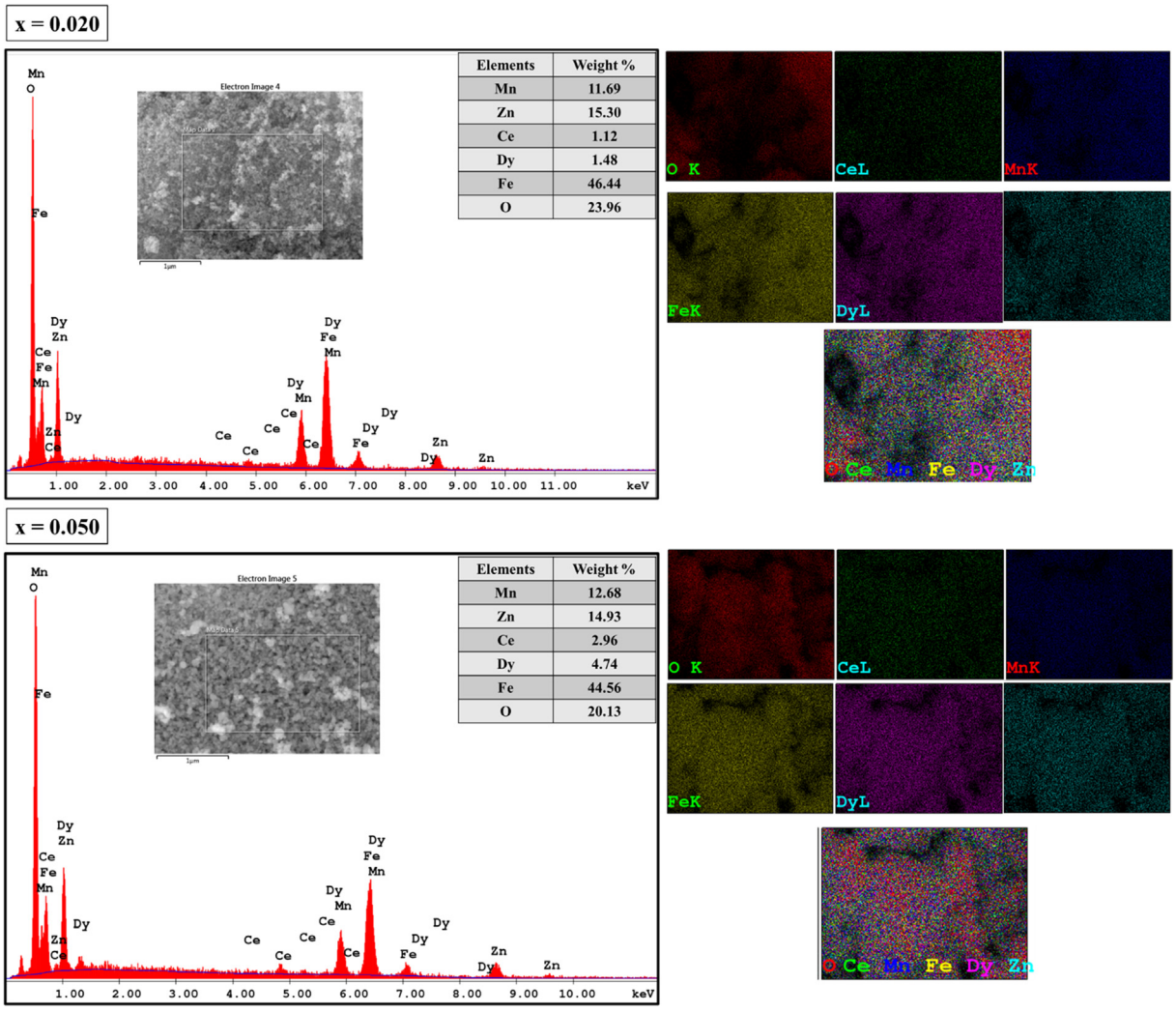

Fig. 4 The EDX spectra and corresponding elemental maps of the synthesized CDMZNSFs (Inset: measured weight% of various elements).

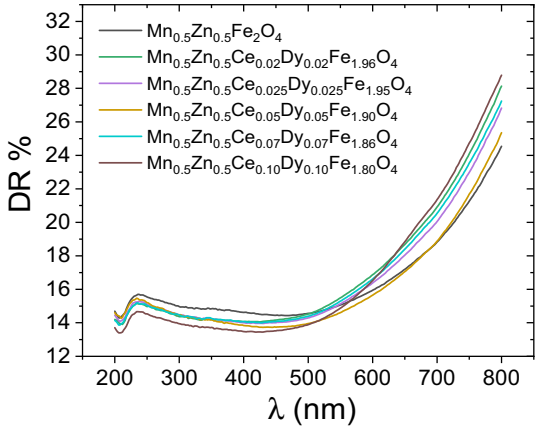

Fig. 5 The diffuse reflectance spectra of the prepared CDMZNSFs.

To further elucidate the magnetic properties of the produced spinel ferrites, the Néel model was employed. The net magnetization (M) of the present spinel ferrites in terms of the A and B sublattice magnetizations (M_A and M_B) yields:

$$M = M_B - M_A \quad (4)$$

The magnetic moments of Mn^{2+}, Zn^{2+}, Fe^{3+}, Ce^{3+} and Dy^{3+} ions are equal to 5, 0, 5, 2.5 and 10.5 μ_B, respectively. Firstly, by assuming only the replacement of some of the Fe^{3+} (5 μ_B) by the Dy^{3+} (10.5 μ_B), an enhancement in the magnetization should be observed, but this is not the case here. In the present study, the value of M_s decreased with the rise in the content of substituting elements. This could be due to the further substitution of some of the Fe^{3+} ions by the Ce^{3+} ions that display a low magnetic moment of 2.5 μ_B. The observed tendency in magnetization can be therefore explained based on the distribution of different cations in the present ferrite crystal structure (i.e. occupation of Mn^{2+}, Zn^{2+}, Fe^{3+}, Ce^{3+}, and Dy^{3+} ions in A and B sites). The cations distribution in the current study showed that the Mn^{2+} and Fe^{3+} ions occupy both A and B-sites, Zn^{2+} ions occupy only A site, and Ce^{3+} and Dy^{3+} ions preferentially to occupied only the B site (Thakur et al., 2020; Mohd Hashim et al., 2018). Conse-

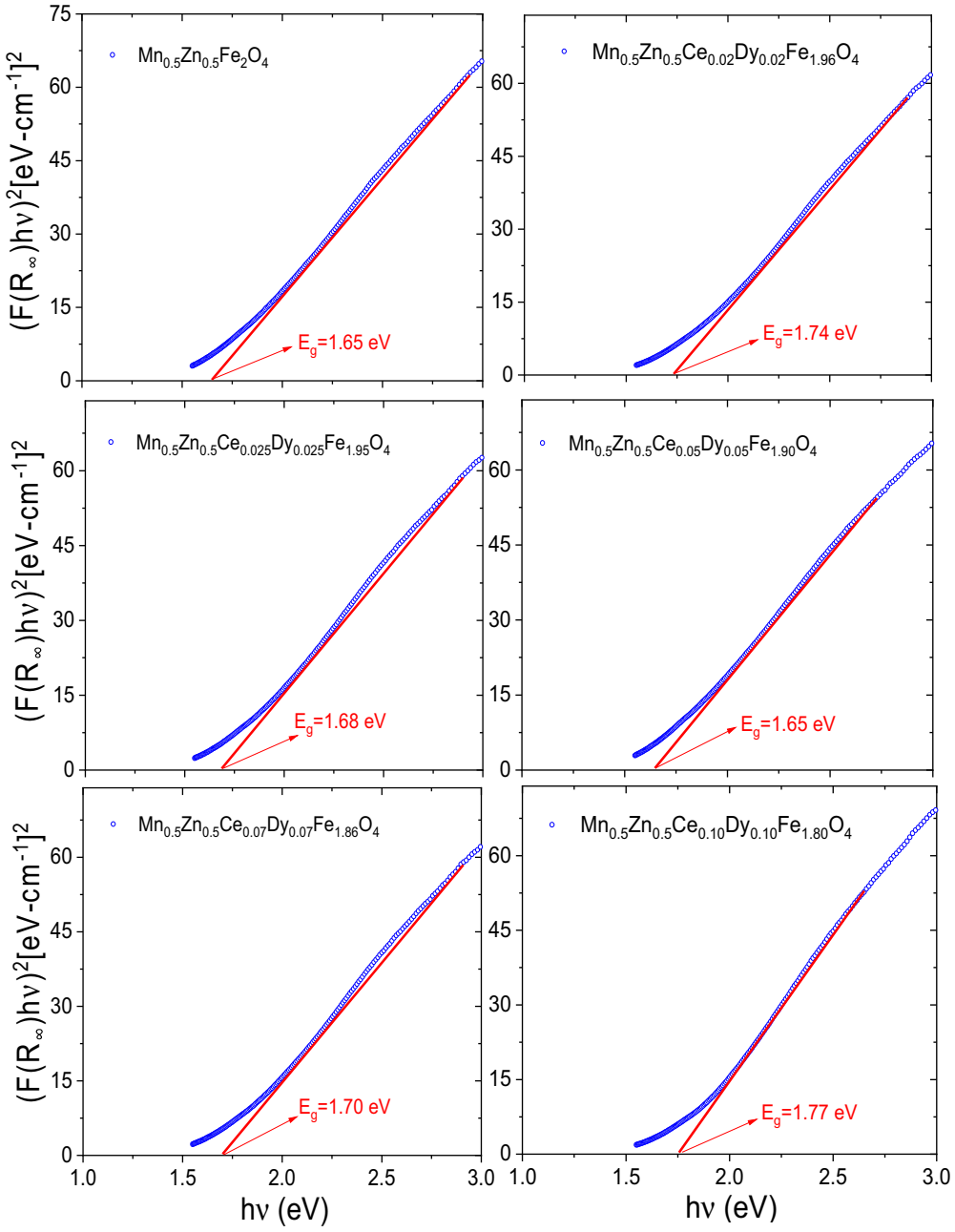

Fig. 6 Tauc plots for all the obtained CDMZNSFs showing the estimated value of the optical band gap energies.

quently, the magnetic moment in the A site is increased with the rise in Dy^{3+} and Ce^{3+} contents, thus reducing the net magnetization of the proposed CDMZNSFs.

3.4.2. Magnetization against temperature (M-T)

Fig. 10 shows the measured ZFC and FC curves (M against T variation) of the produced CDMZNSFs. A splitting and irreversibility are observed in ZFC and FC curves, which is a characteristic of spinel ferrites. In comparison to undoped sample, both M_{ZFC} and M_{FC} values are significantly decreased with the increase in Dy^{3+} and Ce^{3+}contents, which is in line with the M-H results. In addition, the M_{FC} values increased with the decrease in the temperature and reached a maximum value at a certain particular temperature before being dropped. Generally, SPM materials disclose a continuous increase in in the M_{FC} values with the increase in temperature (Peddis et al., 2010). Conversely, an observed plateau-like behavior or a decrement in the M_{FC} value at lower temperatures indicates a transformation in magnetic behavior. Several reports suggested that the emergence of the peak at a particular temperature in the M_{ZFC} versus T curves might be associated to the called blocking temperature (T_B). The blocking temperature (T_B) is a temperature at which the magnetic anisotropy barrier is overcome by the thermal activation, which lead to the fluctuations in magnetization (Pawar et al., 2016). With the increase in the temperature below T_B, the B-site antiferromagnetic interaction becomes stronger. As a consequence, it resulted in a strong spin frustration and a decrease in

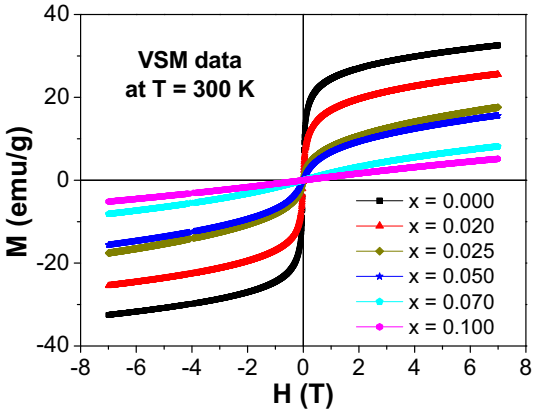

Fig. 7 RT magnetic hysteresis loops (M-H) of all the prepared $(Mn_{0.5}Zn_{0.5})[Fe_{2-2x}Ce_xDy_x]O_4$ NSFs ($0.0 \leq x \leq 0.1$).

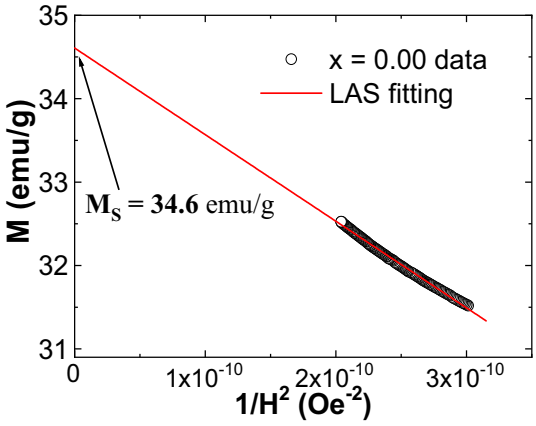

Fig. 8 An example of the M against $1/H^2$ plot of the undoped CDMZNSFs. The solid line shows the LAS fit.

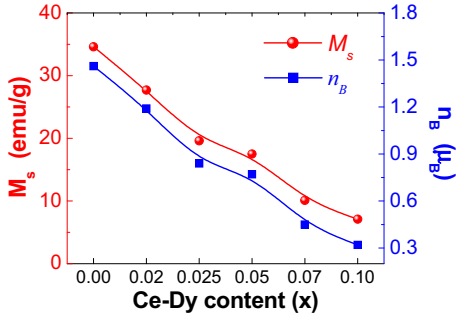

Fig. 9 Variations of M_s and n_B values, for $(Mn_{0.5}Zn_{0.5})[Fe_{2-2x}Ce_xDy_x]O_4$ NSFs ($0.0 \leq x \leq 0.1$), with respect to the content of Ce-Dy co-substituting elements.

magnetization. Above T_B, the thermal energy is higher than the magnetic energy barrier, thus the superparamagnetism appears by following the Curie-Weiss law. Accordingly, the magnetic system is undergoing to a transition from the ferromagnetic (FM) state (under T_B) to the superparmagnetic (SPM) state (above T_B). In the present study, various NSFs disclosed a wide peak at T_B in the M_{ZFC} against T curves, indicating a SPM to FM state transition below T_B. It is clearly noticed that the Ce-Dy substitution with MnZn spinel ferrite significantly influences on the value of T_B. Indeed, the value of T_B shifted from 79.5 K (for the undoped sample) to the lower temperatures with the increase in the content of co-substituting Ce and Dy elements. The values of T_B for the $(Mn_{0.5}Zn_{0.5})[Fe_{2-2x}Ce_xDy_x]O_4$ NSFs with 0.00, 0.02, 0.025, 0.05, 0.07, and 0.10 of Ce^{3+}/Dy^{3+} are discerned to be 79.5, 76.9, 74.8, 74.1, 57.4 and 45.3 K, respectively. Actually, the theory proposed by Néel describes the dependence of the blocking temperature (T_B) on particles size and magneto-crystalline anisotropy constant (K) (Pawar et al., 2016; Humbe et al., 2018). They are related by the following expression:

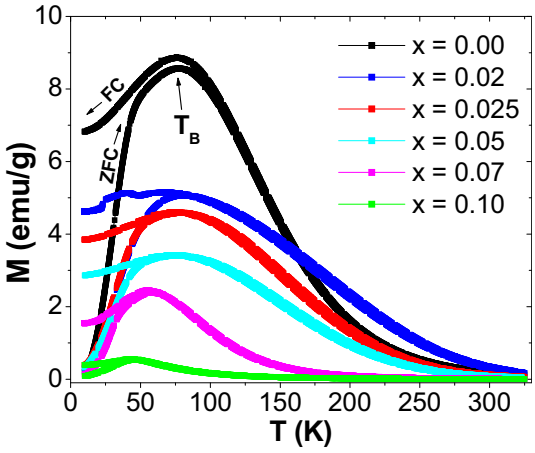

Fig. 10 ZFC-FC magnetizations of the prepared $(Mn_{0.5}Zn_{0.5})[Fe_{2-2x}Ce_xDy_x]O_4$ NSFs ($0.0 \leq x \leq 0.1$) performed under an applied magnetic field of 100 Oe.

$$25k_BT_B = KV \quad (5)$$

where k_B is Boltzmann constant and V is the volume of particles. In the present investigation, the particles/crystallites size decreases with the increase in Ce-Dy content. Accordingly, the decrease in the blocking temperature (T_B) can be attributed to the decrease in particles/crystallites size.

3.5. Anticancer effectiveness

The anticancer activities of the produced CDMZNSFs on the human cells were evaluated via the MTT assay where the inhibitory concentration (IC_{50}) was measured. The 48 h post-treated HCT-116 (cancerous) cells by the CDMZNSFs revealed appreciable inhibition activities, confirming their anti-cancerous benefits for the drug formulation. Table 3 shows the values of IC_{50} obtained by treating the cancel cells by different CDMZNSFs. To verify the cytotoxicity of the proposed CDMZNSFs, they were tested on the healthy human kidney cells (HEK-293). The 48 h post-treated HEK-293 (non-cancerous) cells by the CDMZNSFs did not show any cytotoxic effect, indicating the feasibility of using these NSFs for cancer treatments without damaging the healthy cells.

3.5.1. Cytotoxicity due to nuclear disintegration

Fig. 11 shows the CDMZNSFs-treated HCT-116 (cancer) cells and untreated cells (control group) morphologies after staining

Table 3 The measured IC_{50} values of the CDMZNSFs-treated HCT-116 (cancer) and HEK-293 (normal) human cells.

x	IC_{50} (μg/mL) for HCT-116	IC_{50} (μg/mL) for HEK-293
0.000	0.74	Zero inhibitory action
0.020	0.85	Zero inhibitory action
0.025	0.84	Zero inhibitory action
0.050	0.60	Zero inhibitory action
0.070	0.45	Zero inhibitory action
0.100	2.35	Zero inhibitory action

by DAPI for 48 h. The control (Fig. 11 (a)) did not reveal any inhibition activity. However, the CDMZNSFs-treated (Fig. 11 (a) with the dose of 0.74 μg/mL and Fig. 11 (b) with the dose of 2.35 μg/mL) HCT-116 (cancer) cells exhibited stronger inhibition action (indicated by arrow heads at 200× magnified) compared to the control group, confirming the nuclear staining-mediated loss of the cells.

Present findings indicated that the proposed CDMZNSFs were selective in targeting the colon cancer cells without causing any damage to the noncancerous (normal or healthy) cells, suggesting their prospects for cancer therapeutic purposes. It was acknowledged that the magnetic nanoparticles are beneficial for the drugs delivery and other diagnoses (Qiaoqiao et al., 2019). Furthermore, some reports showed the death of cancerous cells with strong nuclear fragmentations and disintegrations when treated with magnetic nanoparticles, indicating their promise for cancer therapy (Javad et al., 2016; Mytych et al., 2015). In short, the proposed CDMZNSFs revealed strong inhibitory actions on the cancerous cells, indicating their potential for cancer cures.

3.6. Bactericidal activity

3.6.1. MIC/MBC evaluation

The bactericidal efficacy of the as-synthesized CDMZNSFs (at various concentrations from 16 to 0.5 mg/mL) against the *E. coli* and *S. aureus* bacteria was assessed by the values of MIC/MBC. The values of MIC/MBC for the CDMZNSFs-treated *E. coli* bacterial strains were discerned to be 8/16 (for x = 0.00), 8/16 (for x = 0.02), 8/16 (for x = 0.025), 8/16 (for x = 0.05), 4/16 (for x = 0.07) and 4/8 mg/mL (for x = 0.1) as shown in Fig. 12(a). The values of MIC/MBC for the CDMZNSFs-treated *S. aureus* bacterial strains were observed to be 8/16 (for x = 0.00), 8/16 (for x = 0.02), 8/16 (for x = 0.025), 8/16 (for x = 0.05), 8/16 (for x = 0.07) and 4/8 mg/mL (for x = 0.1) as shown in Fig. 12(b). These MIC/MBC indicated the possibility of bactericidal improvement by controlling the Ce^{3+} and Dy^{3+} doping contents in the MZNSFs with the lowest one for x = 0.1. The antibacterial activity of the CDMZNSFs-treated gram-negative bacteria

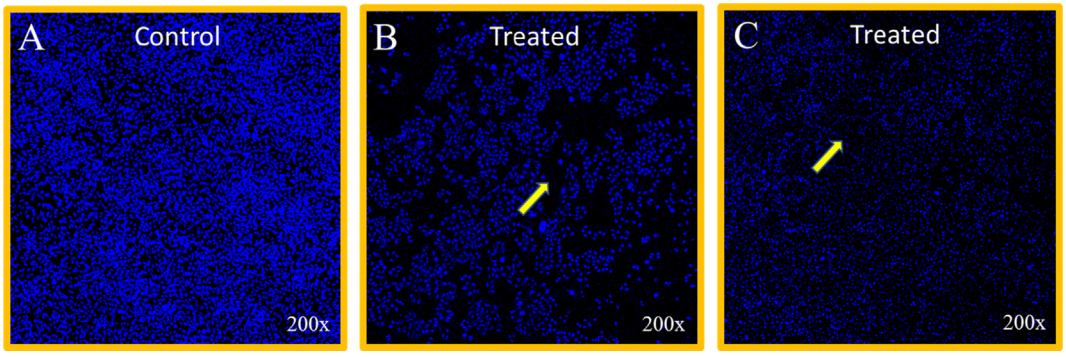

Fig. 11 The cell morphologies after DAPI staining (48 h) for the (a) untreated control group, (b) CDMZNSFs-treated (x = 0.00 dose of 0.74 μg/mL) cancer cells and (c) CDMZNSFs-treated (x = 0.10 dose of 2.35 μg/mL) cancer cells. Arrow heads shows the nuclear staining-mediated decay of the cells.

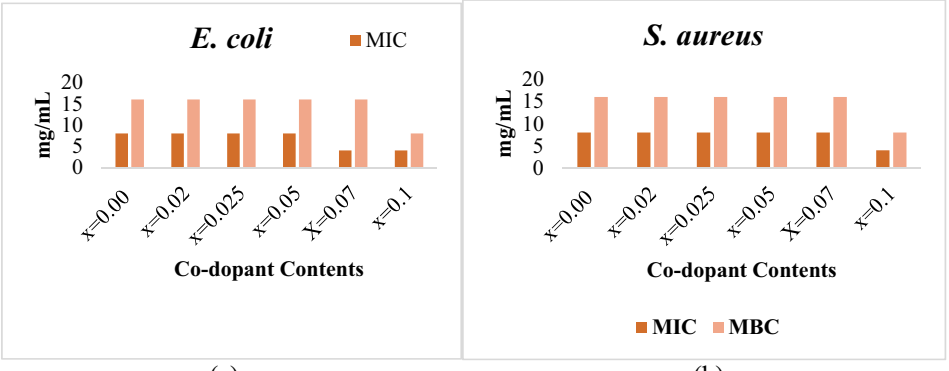

(a) (b)

Fig. 12 The measured values of MIC/MBC for the CDMZNSFs-treated (a) *E.coli,* and (b) *S. aureus* bacteria.

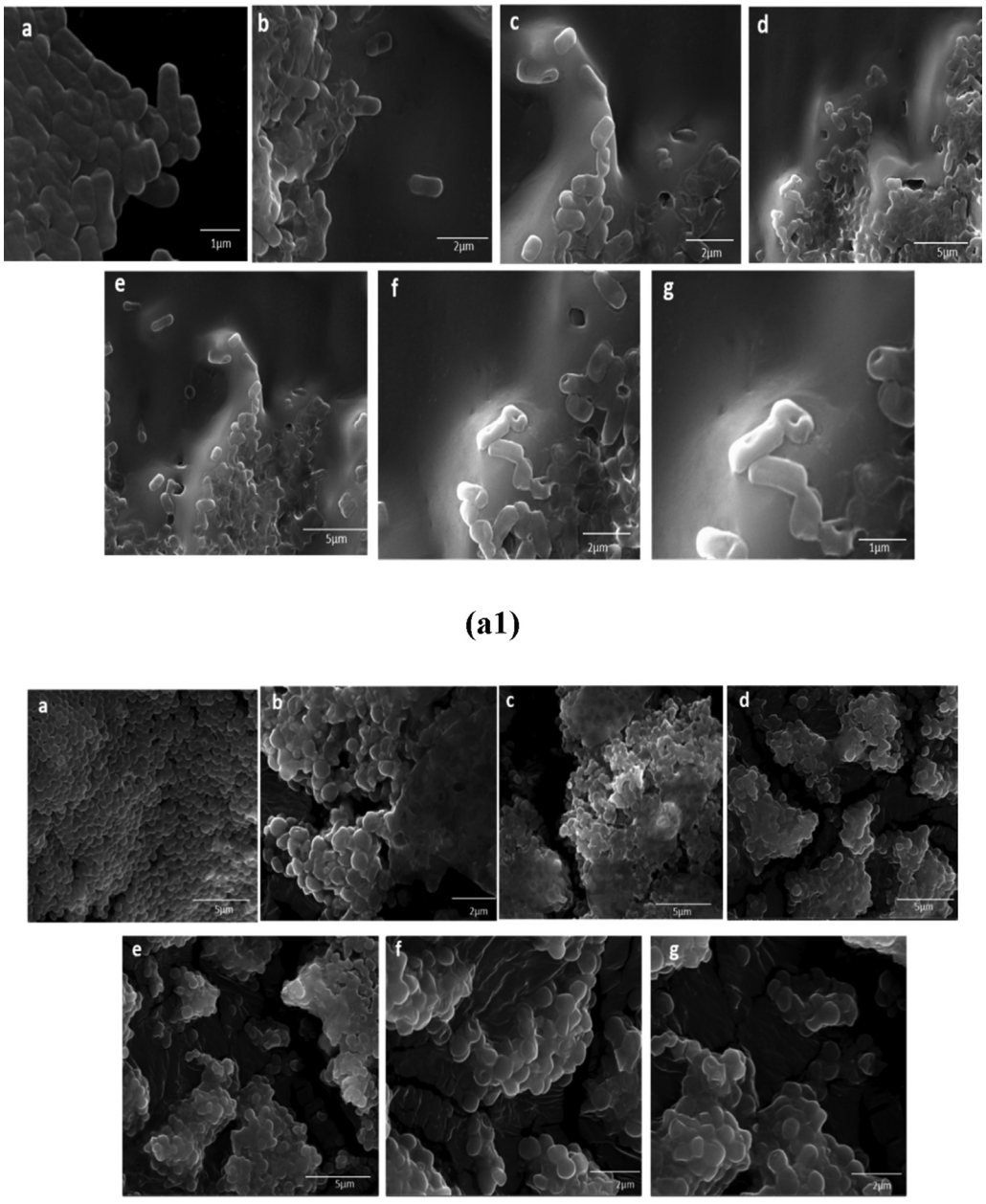

Fig. 13 SEM micrographs of the CDMZNSFs-treated bacteria (**a1)** *E. coli* **(b1)** *S. aureus*. **a)** untreated cells(control), **b)** x = 0.00, **c)** 0.02, **d)** 0.025, **e)** 0.05, **f)** 0.07 and **g)** 0.01.

was slightly higher than the one obtained for the gram-positive bacterial strains that was ascribed to the compositional dissimilarities in their cells wall structures (Rehman et al., 2019; Fekri et al., 2019). The bactericidal potential of various metal ions doped Zn, Cu, Ni and Mn nanoparticles reported in the literature (Asma M et al., 2019; Elsa et al., 2016) are good agreement with the present findings on CDMZNSFs, indicating their prospects for sundry biomedical applications.

3.6.2. Morphologies of CDMZNSFs-treated bacteria

The structural alteration in the *E. coli* and *S. aureus* caused by the CDMZNSFs treatment were examined via SEM imaging. The untreated *E. coli* and *S. aureus* bacterial cells were observed to be normal rod and spherical in shapes with uniform cell surface, respectively (Fig. 13 (a). *E. coli* and *S. aureus* cells treated with x = 0.00 and x = 0.02 showed a mild damage. However, when treated with the CDMZNSFs of x = 0.025 and x = 0.05, the cells were found to be significantly affected (Fig. 13 b, c, d, e). Again, after treating with the CDMZNSFs of x = 0.07 and x = 0.1, the cells were observed to be significantly damaged with a fewer number of cells visible. This damage of the cells with distortion and deformation of the cell surface clearly indicated the loss of integrity of membrane due to the impact of the CDMZNSFs

(Fig. 13 e, f). The cells damage and count of the *E. coli* bacteria was lower compared to the *S. aureus*, which are due to their dissimilar structural compositions of the cells wall (Elsa et al., 2016; de Toledo et al., 2018). It is affirmed that the morphogenesis of both gram negative and gram-positive bacteria was appreciably affected by the CDMZNSFs treatment. This observation was attributed to the efficient attachment and penetration of the CDMZNSFs through the cell membrane, thereby destructing the bacterial cells.

4. Conclusion

This paper evaluated the structure, morphology, optical, magnetic, bactericidal, and anticancer traits of the new series of Ce^{3+}/Dy^{3+} co-activated CDMZNSFs for the first time. These samples were sonochemically prepared and analyzed in-depth. The prepared NSFs manifested a transition from SPM state to FM state below T_B. Both M_s and T_B values were reduced with the rise in Ce^{3+}/Dy^{3+} contents. The variations in various magnetic parameters of the CDMZNSFs as ascribed to the variations in crystallites size and shape, the magnetic moments of substituting ions and host ions, and the cations distribution in the crystal lattice. It was shown that by adjusting the Ce^{3+}/Dy^{3+} co-substituent contents the overall properties of the CDMZNSFs could be tailored. The produced CDMZNSFs revealed appreciable bactericidal (when tested against *E. coli* and *S. aureus* bacteria) and anti-cancerous (tested against cancerous HCT-116 human cells) efficacy. The cancer cells growth was significantly inhibited (with IC_{50} values ranged from 0.74 to 2.35 μg/mL) due to the CDMZNSFs treatment (for 48 h), whereas the normal HEK-293 cells growth was not affected. On top, these CDMZNSFs did not show any cytotoxicity. The MTT assay of the CDMZNSFs-treated cancerous cells disclosed a notable drop in their population, indicating the selective inhibition (DAPI staining for 48 h) of the cancer cells growth by the prepared NSFs. However, the populations of the HEK-293 cells were not affected by the CDMZNSFs treatment. The MIC and MBC displayed realistic bactericidal activity of these NSFs against gram negative and gram-positive bacterial strains. It was established that the proposed Ce^{3+}/Dy^{3+} co-substituted CDMZNSFs can be beneficial for the anti-cancerous and bactericidal applications. In addition, the proposed CDMZNSFs composition may contribute to the development of biomedical and pharmaceutical applications. It is worth to perform more careful studies to validate these disclosures and claim, which is underway. As a future study, microwave absorption properties of Ce^{3+}/Dy^{3+} co-substituted CDMZNSFs will be investigated.

Declaration of Competing Interest

The authors declare there is no conflict of interest.

Acknowledgment

This study is supported by the Institute for Research and Medical Consultations (Project application No. 2018-IRMC-S-2) and by the Deanship for Scientific Research (Project application No. 2020-164-IRMC) of Imam Abdulrahman Bin Faisal University (IAU – Saudi Arabia).

References

Ahmed, M.A., Okasha, N., El-Sayed, M.M., 2007. Enhancement of the physical properties of rare-earth-substituted Mn–Zn ferrites prepared by flash method. Ceram. Int. 33, 49–58.

Akhtar, S., Rehman, S., Almessiere, M.A., Khan, F.A., Slimani, Y., Baykal, A., 2019. Synthesis of $Mn_{0.5}Zn_{0.5}Sm_xEu_xFe_{1.8-2x}O_4$ nanoparticles via hydrothermal approach induced anti-cancer and anti-bacterial activities. Nanomaterials 9 (11), 1635.

Almessiere, M., Korkmaz, A.D., Slimani, Y., Nawaz, M., Ali, S., Baykal, A., 2019. Magneto-optical properties of rare earth metals substituted Co-Zn spinel nanoferrites. Ceram. Int. 45, 3449–3458.

Almessiere, M.A., Slimani, Y., Korkmaz, A.D., Taskhandi, N., Sertkol, M., Baykal, A., Shirsath, S.E., Ercan, İ., Ozçelik, B., 2019b. Sonochemical synthesis of Eu^{3+} substituted $CoFe_2O_4$ nanoparticles and their structural, optical and magnetic properties. Ultrason. Sonochem. 58, 104621.

Almessiere, M.A., Slimani, Y., Sertkol, M., Khan, F.A., Nawaz, M., Tombuloglu, H., Al-Suhaimi, E.A., Baykal, A., 2019. Ce–Nd Co-substituted nanospinel cobalt ferrites: An investigation of their structural, magnetic, optical, and apoptotic properties. Ceram. Int. 45, 16147–16156.

Almessiere, M.A., Slimani, Y., Korkmaz, A.D., Guner, S., Sertkol, M., Shirsath, S.E., Baykal, A., 2019. Structural, optical and magnetic properties of Tm^{3+} substituted cobalt spinel ferrites synthesized via sonochemical approach. Ultrason. Sonochem. 54, 1–10.

Almessiere, M.A., Slimani, Y., Güner, S., Baykal, A., Ercan, I., 2019. Effect of dysprosium substitution on magnetic and structural properties of $NiFe_2O_4$ nanoparticles. J. Rare Earths 37, 871–878.

Almessiere, M.A., Slimani, Y., Kurtan, U., Guner, S., Sertkol, M., Shirsath, S.E., Akhtar, S., Baykal, A., Ercan, I., 2019a. Structural, magnetic, optical properties and cation distribution of nanosized $Co_{0.7}Zn_{0.3}Tm_xFe_{2-x}O_4$ ($0.0 \leq x \leq 0.04$) spinel ferrites synthesized by ultrasonic irradiation. Ultrason. Sonochem. 58, 104638.

Almessiere, M.A., Demir Korkmaz, A., Slimani, Y., Nawaz, M., Ali, S., Baykal, A., 2019. Magneto-optical properties of rare earth metals substituted Co-Zn spinel nanoferrites. Ceram. Int. 45, 3449–3458.

Almessiere, M.A., Trukhanov, A.V., Khan, F.A., Slimani, Y., Tashkandi, N., Turchenko, V.A., Zubar, T.I., Tishkevich, D.I., Trukhanov, S.V., Panina, L.V., Baykal, A., 2020. Correlation between microstructure parameters and anti-cancer activity of the $[Mn_{0.5}Zn_{0.5}](Eu_xNd_xFe_{2-2x})O_4$ nanoferrites produced by modified sol-gel and ultrasonic methods. Ceram. Int. 46, 7346–7354.

Amiri, G.R., Yousefi, M.H., Abolhassani, M.R., Manouchehri, S., Keshavarz, M.H., Fatahian, S., 2011. Magnetic properties and microwave absorption in Ni–Zn and Mn–Zn ferrite nanoparticles synthesized by low-temperature solid-state reaction. J. Magn. Magn. Mater. 323, 730–734.

Asgharzadehahmadi, S., Abdul Raman, A., Parthasarathy, R., Sajjadi, B., 2016. Sonochemical reactors: Review on features, advantages and limitations. Renew. Sustain. Energy Rev. 63 (May).

Ashok, A., Kennedy, L.J., Vijaya, J.J., 2019. Structural, optical and magnetic properties of $Zn_{1-x}Mn_xFe_2O_4$ ($0 \leq x \leq 0.5$) spinel nano particles for transesterification of used cooking oil. J. Alloy. Compd. 780, 816–828.

Asma M, E., Youssef, T.E., Al-Jameel, S.S., Mohamed, H.H., Ansari, M.A., Rehman, S., Akhtar, S., 2019. Synthesis of an activatable tetra-substituted nickel phthalocyanines-4 (3H)-quinazolinone conjugate and its antibacterial activity. Adv. Pharmacol. Sci. Volume 2019 |Article ID 5964687 | 10 pages.

Ateia, E.E., Abdelmaksoud, M.K., Arman, M.M., Shafaay, A.S., 2020. Comparative study on the physical properties of rare-earth-substituted nano-sized $CoFe_2O_4$. Appl. Phys. A 126 (91).

Azadmanjiri, J., 2007. Preparation of Mn–Zn ferrite nanoparticles from chemical sol–gel combustion method and the magnetic properties after sintering. J. Non-Cryst. Solids 353, 4170–4173.

Baykal, A., Güner, S., Demir, A., Esir, S., Genç, F., 2014. Effect of Zinc substitution on magneto-optical properties of $Mn_{1-x}Zn_xFe_2O_4/SiO_2$ nanocomposites. Ceram. Int. 40, 13401–13408.

Baykal, A., Esir, S., Demir, A., Güner, S., 2015. Magnetic and optical properties of $Cu_{1-x}Zn_xFe_2O_4$ nanoparticles dispersed in a silica matrix by a sol-gel auto-combustion method. Ceram. Int. 41, 231–239.

Baykal, A., Güner, S., Demir, A., 2015. Synthesis and magneto-optical properties of triethylene glycol stabilized $Mn_{1-x}Zn_x Fe_2O_4$ nanoparticles. J. Alloy. Compd. 619, 5–11.

Baykal, A., Esir, S., Demir, A., Güner, S., 2015. Magnetic and optical properties of $Cu_{1-x}Zn_xFe_2O_4$ nanoparticles dispersed in a silica matrix by a sol–gel auto-combustion method. Ceram. Int. 41, 231–239.

Baykal, A., Guner, S., Gungunes, H., Batoo, K.M., 2018. Md Amir, A Manikandan, Magneto Optical Properties and Hyperfine Interactions of Cr^{3+} Ion Substituted Copper Ferrite Nanoparticles. J. Inorg. Organo. Polym. Mater. 28, 2533–2544.

Blitz, John P., 1998. Diffuse Reflectance Spectroscopy, Modern Techniques in Applied Molecular Spectroscopy, John Wiley & Sons, Inc., 1998. ISBN 0-471-12359-5 © (Chapter 5)

Chand, M., Kumar, A., Annveer, S., Kumar, A., Shankar, R.P.P., 2011. Investigations on MnxZn1-xFe2O4 (x = 0.1, 0.3 and 0.5) nanoparticles synthesized by sol-gel and co-precipitation methods. Ind. J. Eng. Mater. Sci. 18, 385.

Coey, J.M.D., 1971. Noncollinear spin arrangement in ultrafine ferrimagnetic crystallites. Phys. Rev. Lett. 27, 1140–1142.

de Toledo, Lucas, de Alcantara Sica, H.C., Rosseto, M.L. Bruschi, 2018. Iron oxide magnetic nanoparticles as antimicrobials for therapeutics. Pharm. Dev. Technol. 23, 316–323.

Demir, A., Güner, S., Bakıs, Y., Esir, S., Baykal, A., 2014. Magnetic and optical properties of $Mn_{1-x}Zn_xFe_2O_4$ nanoparticles. J. Inorg. Organometall. Polym. Mater. 24, 729–736.

Elsa, C., Rajan, A., Baskar, G., 2016. Synthesis of manganese dioxide nanoparticles using co-precipitation method and its antimicrobial activity. Int. J. Modern Sci. Technol. 1, 17–22.

Eskandari, N., Nabiyouni, G., Masoumi, S., Ghanbari, D., 2019. Preparation of a new magnetic and photo-catalyst $CoFe_2O_4$–$SrTiO_3$ perovskite nanocomposite for photo-degradation of toxic dyes under short time visible irradiation. Compos. B Eng. 176, 107343.

Etminan, M., Nabiyouni, G., Ghanbari, D., 2018. Preparation of tin ferrite–tin oxide by hydrothermal, precipitation and auto-combustion: photo-catalyst and magnetic nanocomposites for degradation of toxic azo-dyes. J. Mater. Sci.: Mater. Electron. 29, 1766–1776.

Fekri, A., Ahmed, A., Alam, J., Shukla, A.K., Alhoshan, M., Ansari, M.A., Al-Masry, W.A., Rehman, S., Alam, M., 2019. Evaluation of antibacterial and antifouling properties of silver-loaded GO polysulfone nanocomposite membrane against Escherichia coli, Staphylococcus aureus, and BSA protein. React. Funct. Polym. 140, 136–147.

Gabal, M.A., Abdel-Daiem, A.M., Al Angari, Y.M., Ismail, I.M., 2013. Influence of Al-substitution on structural, electrical and magnetic properties of Mn–Zn ferrites nanopowders prepared via the sol–gel auto-combustion method. Polyhedron 57, 105–111.

Güner, S., Amir, M.d., Geleri, M., Sertkol, M., Baykal, A., 2015. Magneto-optical properties of Mn^{3+} substituted Fe_3O_4 nanoparticles. Ceram. Int. 41, 10915–10922.

Hashim, M., Ahmed, A., Ali, S.A., Shirsath, S.E., Ismail, M.M., Kumar, R., Kumar, S., Meena, S.S., Ravinder, D., 2020. Structural, optical, elastic and magnetic properties of Ce and Dy doped cobalt ferrites. J. Alloy. Compd. 834, 155089.

Hu, P., Yang, H.B., Pan, D.A., Wang, H., Tian, J.J., Zhang, S.G., Wang, X.F., Volinsky, A.A., 2010. Heat treatment effects on microstructure and magnetic properties of Mn-Zn ferrite powders. J. Magn. Magn. Mater. 322, 173–177.

Humbe, Ashok V., Kounsalye, Jitendra S., Shisode, Mahendra V., Jadhav, K.M., 2018. Rietveld refinement, morphology and superparamagnetism of nanocrystalline Ni0.70−xCuxZn0.30Fe2O4 spinel ferrite. Ceram. Int. 44, 5466–5472.

Isfahani, M.J.N., Myndyk, M., Menzel, D., Feldhoff, A., Amighian, J., Šepelák, V., 2009. Magnetic properties of nanostructured MnZn ferrite. J. Magn. Magn. Mater. 321, 152–156.

Islam, R., Hakim, M.A., Rahman, M.O., Narayan Das, H., Mamun, M.A., 2013. Study of the structural, magnetic and electrical properties of Gd-substituted Mn–Zn mixed ferrites. J. Alloy. Compd. 559, 174–180.

Javad, B., Ramezani, T., Divsalar, A., Mousavi, M., Seyedarabi, A., 2016. Induction of apoptosis by green synthesized gold nanoparticles through activation of caspase-3 and 9 in human cervical cancer cells. Avicenna J. Med. Biotechnol. 8, 75.

Joulaei, M., Hedayati, K., Ghanbari, D., 2019. Investigation of magnetic, mechanical and flame retardant properties of polymeric nanocomposites: Green synthesis of $MgFe_2O_4$ by lime and orange extracts. Compos. B Eng. 176, 107345.

Kadam, A.A., Shinde, S.S., Yadav, S.P., Patil, P.S., Rajpure, K.Y., 2013. Structural, morphological, electrical and magnetic properties of Dy doped Ni–Co substitutional spinel ferrite. J. Magn. Magn. Mater. 329, 59–64.

Kiani, A., Nabiyouni, G., Masoumi, S., Ghanbari, D., 2019. A novel magnetic $MgFe_2O_4$–$MgTiO_3$ perovskite nanocomposite: Rapid-photo-degradation of toxic dyes under visible irradiation. Compos. B Eng. 175, 107080.

Kogias, G., Zaspalis, V.T., 2016. Temperature stable MnZn ferrites for applications in the frequency region of 500 kHz. Ceram. Int. 42, 7639–7646.

Lazarević, Z.Ž., Jovalekić, Č., Milutinović, A., Sekulić, D., Ivanovski, V.N., Rečnik, A., et al, 2013. Nanodimensional spinel $NiFe_2O_4$ and $ZnFe_2O_4$ ferrites prepared by soft mechanochemical synthesis. J. Appl. Phys. 113, 187221.

Li, L.Z., Zhong, X.X., Wang, R., Tu, X.Q., He, L., Wang, F.H., 2019. Effects of Ce substitution on the structural and electromagnetic properties of NiZn ferrite. J. Magn. Magn. Mater. 475, 1–4.

Mathur, P., Thakur, A., Singh, M., 2007. Study of low-temperature sintered nano-crystalline Mn-Cu-Zn ferrite prepared by co-precipitation method. Modern Phys. Lett. B 21, 1425–1430.

Modak, S., Ammar, M., Mazaleyrat, F., Das, S., Chakrabarti, P.K., 2009. XRD, HR-TEM and magnetic properties of mixed spinel nanocrystalline Ni-Zn-Cu-ferrite. J. Alloy. Compd. 473, 15–19.

Mohd Hashim, M., Raghasudha, Sher Singh, Meena, Jyoti Shah, Shirsath, Sagar E., Shalendra Kumar, D., Ravinder, Pramod Bhatt, Alimuddin, Ravi Kumar, Kotnala, R.K., 2018. Influence of rare earth ion doping (Ce and Dy) on electrical and magnetic properties of cobalt ferrites. J. Magn. Magn. Mater. 449, 319–327.

Moradi, B., Nabiyouni, G., Ghanbari, D., 2018. Rapid photo-degradation of toxic dye pollutants: green synthesis of monodisperse Fe_3O_4–CeO_2 nanocomposites in the presence of lemon extract. J. Mater. Sci.: Mater. Electron. 29, 11065–11080.

Mytych, J., Anna, L., Jacek, Z., Maciej, W., 2015. Gold nanoparticles promote oxidant-mediated activation of NF-κB and 53BP1 recruitment-based adaptive response in human astrocytes. BioMed Res. Int.

Naghikhani, R., Nabiyouni, G., Ghanbari, D., 2018. Simple and green synthesis of $CuFe_2O_4$–CuO nanocomposite using some natural extracts: photo-degradation and magnetic study of nanoparticles. J. Mater. Sci.: Mater. Electron. 29, 4689–4703.

Nairan, Adeela, Khan, Maaz, Khan, Usman, Iqbal, Munawar, Riaz, Saira, Naseem, Shahzad, 2016. Temperature-dependent magnetic response of antiferromagnetic doping in cobalt ferrite nanostructures. Nanomaterials 6, 73.

Nam, P.H., Phuc, N.X., Linh, P.H., Lu, L.T., Manh, D.H., Phong, P. T., 2018. In-JaLee, Effect of zinc on structure, optical and magnetic

properties and magnetic heating efficiency of $Mn_{1-x}Zn_xFe_2O_4$ nanoparticles. Phys. B Cond. Matter. 550, 428–435.
Parekh, K., Upadhyay, R.V., Belova, L., Rao, K.V., 2006. Ternary monodispersed $Mn_{0.5}Zn_{0.5}Fe_2O$ 4 ferrite nanoparticles: preparation and magnetic characterization. Nanotechnology 17, 5970–5975.
Parvatheeswara Rao, B., Kim, C.-O., Kim, C.G., Dumitru, I., Spinu, L., Caltun, O.F., 2006. Structural and magnetic characterizations of coprecipitated Ni–Zn and Mn–Zn ferrite nanoparticles. IEEE Trans. Magn. 42, 2858.
Pawar, R.A., Patange, S.M., Shirsath, S.E., 2016. Spin glass behavior and enhanced but frustrated magnetization in Ho3+ substituted Co-Zn ferrite interacting nanoparticles. RSC Adv. 6, 76590–76599.
Peddis, D., Cannas, C., Piccaluga, G., Agostinelli, E., Fiorani, D., 2010. Surface spin freezing effects on enhanced saturation magnetization and magnetic anisotropy in $CoFe_2O_4$ nanoparticles. Nanotechnology 21, 125705.
Pinjari, D.V., Pandit, A.B., 2011. Room temperature synthesis of crystalline CeO_2 nanopowder: Advantage of sonochemical method over conventional method. Ultrason. Sonochem. 18 (5), 1118–1123.
Qiaoqiao, Z., Yang, X., Guan, J., 2019. Applications of Magnetic Nanomaterials in Heterogeneous Catalysis. ACS Appl. Nano Mater. 2, 4681–4697.
Ranjith Kumar, E., Jayaprakash, R., Seehra, M.S., Prakash, T., Kumar, Sanjay, 2013. Effect of α-Fe_2O_3 phase on structural, magnetic and dielectric properties of Mn–Zn ferrite nanoparticles. J. Phys. Chem. Solids 74, 943–949.
Rath, C., Sahu, K.K., Anand, S., Date, S.K., Mishra, N.C., Das, R.P., 1999. Preparation and characterization of nanosize Mn–Zn ferrite. J. Magn. Magn. Mater. 202, 77–84.
Rehman, S., Ansari, M.A., Alzohairy, M.A., Alomary, M.N., Jermy, B.R., Shahzad, R., Tashkandi, N., Alsalem, Z.H., 2019. Antibacterial and antifungal activity of novel synthesized neodymium-substituted cobalt ferrite nanoparticles for biomedical application. Processes 7, 714.
Rehman, S., Almessiere, M.A., Korkmaz, A.D., Natashakandi, N., Slimani, Y., Baykal, A., 2020. Synthesis and biological characterization of $Mn_{0.5}Zn_{0.5}Eu_xDy_xFe_{1.8-2x}O_4$ nanoparticles by sonochemical approach. Mater. Sci. Eng., C 109, 110534.
Rezlescu, N., Rezlescu, E., Popa, D.P., Rezlescu, L., 1998. Effects of rare-earth oxides on physical properties of Li–Zn ferrite. J. Alloy. Compd. 275–277, 657.
Shirsath, S.E., Jadhav, S.S., Toksha, B.G., Patange, S.M., Jadhav, K. M., 2011. Influence of Ce4+ ions on the structural and magnetic properties of NiFe2O4. J. Appl. Phys. 110. 013914-1-8.
Shirsath, S.E., Mane, M.L., Yasukawa, Y., Liu, X., Morisako, A., 2013. Chemical tuning of structure formation and combustion process in $CoDy_{0.1}Fe_{1.9}O_4$ nanoparticles: influence@pH. J. Nanopart. Res. 15, 1976.
Shirsath, S.E., Mane, M.L., Yasukawa, Y., Liu, X., Morisakoa, A., 2014. Self-ignited high temperature synthesis and enhanced super-exchange interactions of Ho^{3+}–Mn^{2+}–Fe^{3+}–O^{2-} ferromagnetic nanoparticles. PCCP 16, 2347–2357.
Shirsath, S.E., Wang, D., Jadhav, S.S., Mane, M.L., Li, S., 2018. Ferrites obtained by sol-gel method. In: Klein, L., Aparicio, M., Jitianu, A. (Eds.), Handbook of Sol-Gel Science and Technology. Springer, Cham, pp. 695–735.
Slimani, Y., Güngüneş, H., Nawaz, M., Manikandan, A., El Sayed, H., Almessiere, M., Sözeri, H., Shirsath, S., Ercan, I., Baykal, A., 2018. Magneto-optical and microstructural properties of spinel cubic copper ferrites with Li-Al co-substitution. Ceram. Int. 44, 14242–14250.
Slimani, Y., Almessiere, M., Nawaz, M., Baykal, A., Akhtar, S., Ercan, I., Belenli, I., 2019. Effect of bimetallic (Ca, Mg) substitution on magneto-optical properties of $NiFe_2O_4$ nanoparticles. Ceram. Int. 45, 6021–6029.
Song, J., Wang, L., Xu, N., Zhang, Q., 2010. Microwave electromagnetic and absorbing properties of Dy^{3+} doped MnZn ferrites. J. Rare Earths 28 (3), 451–455.
Stoner, E.C., Wohlfarth, E., 1948. A mechanism of magnetic hysteresis in heterogeneous alloys. Philos. Trans. R Soc. Lond. Ser. A Math. Phys. Sci. 240, 599–642.
Tauc, J., Grigorovici, R., Vancu, A., 1966. Optical properties and electronic structure of amorphous germanium. Physica Status Solidi 15, 627–637.
Thakur, Preeti, Chahar, Deepika, Taneja, Shilpa, Bhalla, Nikhil, Thakurc, Atul, 2020. A review on MnZn ferrites: synthesis, characterization and applications. Ceram. Int. 46, 15740–15763.
Topfer, J., Angermann, A., 2011. Nanocrystalline magnetite and Mn-Zn ferrite particles via the polyol process: synthesis and magnetic properties. Mater. Chem. Phys. 129, 337–342.
Xing, Q., Peng, Z., Wang, C., Fu, Z., Fu, X., 2012. Doping effect of Y^{3+} ions on the microstructural and electromagnetic properties of Mn–Zn ferrites. Phys. B Cond. Matter. 407 (3), 388–392.
Zhang, C.F., Zhong, X.C., Yu, H.Y., Liu, Z.W., Zeng, D.C., 2009. Effects of cobalt doping on the microstructure and magnetic properties of Mn–Zn ferrites prepared by the co-precipitation method. Phys. B Cond. Matter. 404, 2327.